Active Evaluation-Induced Graph Network Based Medical Hyperspectral Image Classification for Tumor Diagnosis

Meiling Wang[1], Changda Xing[2](✉), Yifang Wu[2], and Liying Cao[2]

[1] School of Computer Science, Nanjing University of Posts and Telecommunications, Nanjing, China
mely@njupt.edu.cn

[2] School of Information and Control Engineering, China University of Mining and Technology, Xuzhou, China
{xingchangda,ts24060257p31,ts24060205p31}@cumt.edu.cn

Abstract. Graph networks (GNet) have presented great potential in medical hyperspectral images (MedHSIs) for tumor diagnosis. Most of existing approaches easily suffer from the misconnection of graph internodes due to tissue heterogeneity, imaging noise, and spectral aliasing included in MedHSIs. To remedy such difficulty, a novel active evaluation-induced graph network (AEGNet) based MedHSI classification is proposed for tumor diagnosis. The main innovative contributions are twofold. (1) Active Evaluation Scheme: We introduce an adversarial discriminator to actively evaluate and refine the correlations (edges) between nodes, enabling more precise graph construction. (2) Hierarchical Calibration Loss: To mitigate the hierarchical misalignment caused by potential inter-node misconceptions, we design a hierarchical calibration loss that enforces consistency between the features of all hidden layers and those of the final layer, improving feature representation across the network. In our experiments, complete empirical evidence has been provided on the *In Vivo Hyperspectral Human Brain* database, demonstrating that the proposed AEGNet method surpasses several representative approaches in the MedHSI classification based tumor diagnosis task. The ablation discussion has been provided to experimentally reveal the effectiveness of the innovative active evaluation and hierarchical calibration.

Keywords: Medical hyperspectral image classification· Tumor diagnosis · Graph network · Active evaluation.

1 Introduction

Medical hyperspectral imaging (MedHSI) guided techniques have demonstrated significant promise in tumor diagnosis, which is capable of simultaneously capturing two-dimensional spatial and one-dimensional spectral information from biological tissues, spanning spectral regions such as visible light, infrared, and ultraviolet. With its high spectral resolution, MedHSI provides diagnostic insights into tissue physiology, morphology, and biochemical composition, offering

more nuanced spectral features for histological research and supplementary data for medical pathological diagnosis.

Recently, deep learning has been successfully introduced to automatically analyze spectral signatures to discern pathological characteristics [11, 17, 19, 5, 10, 14, 7, 8, 6, 20, 16, 13], which enables the identification of pathological tissues or structures. These methods are adept at uncovering the high-order latent information hidden within MedHSI data and subsequently fitting decision boundaries for tumor diagnosis. Halicek et al. [5] introduced a convolutional neural network (CNN)-based classifier to categorize excised tissue samples, including squamous cell carcinoma, thyroid cancer, and normal head and neck tissues, within the MedHSI framework. Empirical results from 50 patients demonstrated the significant potential of CNN-based MedHSI analysis for the automated labeling of surgical specimens from head and neck patients. Similarly, Li et al. [10] employed a CNN architecture to accurately distinguish blood cells in MedHSI data. Further advancing the field, Hao et al. [6] developed a fused multiple deep model (FMDM) to recognize glioblastoma tumors by classifying human brain MedHSIs. Zeng et al. [20] introduced a fusion transformer with parallel CNN (FUST) for microscopic MedHSI classification. In scenarios involving unlabeled data, auto-encoders (AEs) have shown considerable promise in recent years. Wei et al. [16], for example, employed an unsupervised two-channel AE to jointly learn spatial-spectral features for blood cell classification. Wang et al. [13] proposed a deep margin cosine auto-encoder (DMCA) framework for tumor diagnosis using MedHSI. These approaches reviewed-above have shown highly competitive performance in hyperspectral tumor diagnosis through empirical validation.

Owing to shared imaging principles, many remote sensing related techniques have been directly transferred to MedHSI tasks for hyperspectral tumor diagnosis [13]. Consequently, beyond CNNs and AEs, other deep architectures [15, 9, 18] are also being leveraged in hyperspectral tumor diagnosis, among which graph networks (GNet) [4, 2, 1] serve as a prime example. In the GNet related models, the pixels or features are considered as nodes in the graph structure and edges are built by spatial-spectral relationships between nodes. For instance, Wang et al. [15] proposed a weak-strong graph contrastive learning (WSGraphCL) model for HSI classification. Jia et al. [9] designed a graph-in-graph (GiG) model and a related GiG convolutional network (GiGCN) for HSI classification from a superpixel viewpoint, which covers information inside and outside superpixels, respectively, corresponding to the local and global characteristics of objects. Most of the aforementioned reviewed GNet methods have presented tremendous potential in hyperspectral tumor diagnosis. However, traditional graph construction methods usually presuppose strong correlations among nodes, often establishing edges based on spatial closeness or fixed spectral thresholds. Because of tissue heterogeneity, imaging noise, and spectral aliasing included in MedHSIs, similar tissues may exhibit substantial spectral disparities, while dissimilar tissues may appear alike, which can result in misconnecting tumors with normal tissues.

Our contributions: We propose a novel active evaluation-induced graph network (AEGNet) based MedHSI classification for tumor diagnosis, with the

overall framework visually shown in Fig. 1. Our method adopts a GNet as the foundational backbone to perform graph representation learning and diagnostic prediction. To address the challenge of inaccurate inter-node correlation modeling, we introduce an adversarial discriminator that actively evaluates the authenticity of node relationships and dynamically determines the existence of edges, thereby enabling more precise graph construction. Furthermore, to mitigate hierarchical misalignment potentially caused by such inter-node misconceptions, we design a hierarchical calibration loss that enforces consistency between the hidden features of all layers and those of the final layer, promoting robust feature learning throughout the network. Extensive experiments demonstrate that the proposed AEGNet outperforms several representative methods in the hyperspectral tumor diagnosis task, and ablation studies validate the effectiveness of both the active evaluation mechanism and the hierarchical calibration loss.

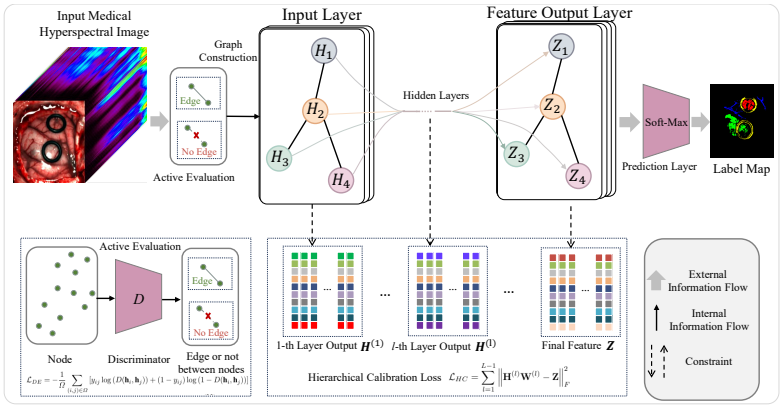

Fig. 1. Overall framework of the proposed active evaluation-induced graph network (AEGNet) based MedHSI classification for tumor diagnosis.

2 Methodology

2.1 Problem Set-up

Foundational Architecture: We here define $\mathbf{X} \in \mathbb{R}^{N \times d}$ as the input MedHSI matrix, where N is the number of pixels and d is the amount of spectral bands. Given a GNet with L layers, the foundational architecture is constructed to learn adjacent matrix $\mathbf{A} \in \mathbb{R}^{N \times N}$ representing graph structure, whose propagation rule for each layer is as follows:

$$\mathbf{H}^{(l+1)} = \sigma\left(\hat{\mathbf{D}}^{-\frac{1}{2}}\hat{\mathbf{A}}\hat{\mathbf{D}}^{-\frac{1}{2}}\mathbf{H}^{(l)}\Theta^{(l)}\right), \tag{1}$$

where $\hat{\mathbf{A}} = \mathbf{A} + \mathbf{I}$ is used to add self-loops; $\hat{\mathbf{D}}$ is the degree matrix of $\hat{\mathbf{A}}$, i.e., $\hat{\mathbf{D}}_{ii} = \sum_j \hat{\mathbf{A}}_{ij}$; $\Theta^{(l)}$ denotes the weight matrix at the l-th layer; σ is the activation

function with rectified linear unit (ReLU); $\mathbf{H}^{(l)}$ is the feature matrix at the lth layer, where $\mathbf{H}^{(0)} = \mathbf{X}$.

Active Evaluation: Conventional graph construction generally assumes strong correlations between nodes, such as directly building edges based on spatial proximity or fixed spectral thresholds. However, in MedHSIs, due to tissue heterogeneity, imaging noise, and spectral aliasing, similar tissues may have significant spectral differences, while dissimilar tissues may be similar, which may lead to misconnections (such as misconnecting tumors with normal tissues). Error edges can disrupt the semantic structure of the graph, so as to confuse features during message transmission and reduce the clarity of decision boundaries. Overall, actively dynamically evaluating the edges between nodes is conducive to more accurate graph construction. For this purpose, we introduce an adversarial discriminator to achieve the dynamic evaluation of the correlation between nodes. Here, positive and negative samples are required to train the discriminator, where positive samples are the pairs of intra-class nodes and negative samples are those of inter-class nodes. Thus, the loss of active evaluation is written into the following binary cross-entropy:

$$\mathcal{L}_{DE} = -\frac{1}{\Omega} \sum_{(i,j)\in\Omega} \left[y_{ij} \log \left(D(\mathbf{h}_i, \mathbf{h}_j) \right) + (1 - y_{ij}) \log \left(1 - D(\mathbf{h}_i, \mathbf{h}_j) \right) \right], \tag{2}$$

where $y_{ij} = 1$ if node i and node j are from the same class, otherwise $y_{ij} = 0$; Ω denotes the set of edges for training; $D(\mathbf{h}_i, \mathbf{h}_j)$ is the output of active dynamic evaluation. Once being trained, we use the $D(\mathbf{h}_i, \mathbf{h}_j)$ as the edge weight between $\mathbf{h}_i$ and $\mathbf{h}_j$, i.e.,

$$\mathbf{A}_{ij} = D(\mathbf{h}_i, \mathbf{h}_j). \tag{3}$$

This dynamically optimized graph structure, refined through adversarial evaluation and regularization, better reflects true node correlations. By pruning noisy edges and reinforcing meaningful connections, it guides message propagation along reliable paths. Consequently, this enhances feature consistency across layers, sharpens decision boundaries, and improves the model's robustness against heterogeneous noise in MedHSIs.

We further impose the L1 regularization and graph laplacian regularization on the learned graph structure. Therefore, the regularization loss of graph structure is:

$$\mathcal{L}_{GP} = \|\mathbf{A}\|_1 + \lambda \mathrm{tr} \left(\mathbf{Z}^T \mathbf{L} \mathbf{Z} \right), \tag{4}$$

where λ is a hyperparameter; $\|\mathbf{A}\|_1$ is used to guarantee the sparsity; $\mathrm{tr} \left(\mathbf{Z}^T \mathbf{L} \mathbf{Z} \right)$ aims to embrace the smoothness.

Hierarchical Calibration: The correctness of node connections (i.e., the quality of the graph structure) directly affects the distribution of features across layers. Misconnections can exacerbate or even directly lead to feature misalignment. Therefore, we need to find a way to guarantee the consistency between all hidden features and the features of the final layer. We here introduce a hierarchical calibration loss to encourage all hidden features to remain consistent with

the features of the final layer, i.e.,

$$\mathcal{L}_{HC} = \sum_{l=1}^{L-1} \left\| \mathbf{H}^{(l)}\mathbf{W}^{(l)} - \mathbf{Z} \right\|_F^2, \tag{5}$$

where $\mathbf{W}^{(l)}$ is the linear transformation matrix, which guarantees the semantic consistency by mapping the feature at the l-th layer into the dimension space of the final feature $\mathbf{Z}$. By enforcing alignment between intermediate hidden features and the final layer representation, the hierarchical calibration loss acts as a form of deep supervision. It encourages each layer to progressively refine its features toward the final semantic space, mitigating issues like over-smoothing and gradient vanishing in deep graph networks. Even when the graph structure contains noisy or misconnected edges, this consistency constraint helps stabilize the feature distributions across layers, preventing the accumulation of irrelevant information. Moreover, the linear transformations $\mathbf{W}^{(l)}$ ensure that features from different layers are projected into a common subspace, facilitating direct comparisons and fusion. This not only enhances the robustness of the learned representations but also promotes more discriminative hierarchical features, ultimately improving performance on downstream tasks such as node classification and link prediction.

Overall Loss: According to the mentioned-above, the overall loss can be written into:

$$\mathcal{L} = \mathcal{L}_{CL} + \alpha\mathcal{L}_{HC} + \beta\mathcal{L}_{DE} + \gamma\mathcal{L}_{GP}, \tag{6}$$

where α, β, and γ are three coupling parameters. $\mathcal{L}_{CL}$ denotes the class loss used for result prediction, which can be mathematically described into:

$$\mathcal{L}_{CL} = -\frac{1}{|S|} \sum_{i \in S} \sum_{c=1}^{C} \mathbf{Y}_{ic} \log \left(\text{softmax}(\mathbf{Z}_i)_c \right), \tag{7}$$

where S is a labeled training sample set; Y_{ic} is the one-hot representation of the true label. If node i belongs to category c, then $Y_{ic} = 1$, otherwise $Y_{ic} = 0$; $\text{softmax}(\mathbf{Z}_i)$ is used to convert each row of $\mathbf{Z}$ into a probability distribution as following:

$$\text{softmax}(\mathbf{Z}_i) = \frac{\mathbf{Z}_i}{\sum_{c=1}^{C} \exp(\mathbf{Z}_{ic})}, \tag{8}$$

where $\mathbf{Z} \in \mathbb{R}^{N \times C}$ is the final features, and C denotes the number of classes included in MedHSI.

2.2 Training Strategy

The training strategy for the overall loss in Eq. (6) is achieved by using an alternating direction-based optimization scheme. The procedure iteratively updates the network parameters Θ, the discriminator parameters Φ, the graph structure $\mathbf{A}$, the transformation matrices $\{\mathbf{W}^{(l)}\}$, the auxiliary variable $\mathbf{B}$, and the Lagrange multiplier Λ. In summary, this iterative process decouples the complex

joint optimization into simpler sub-problems, enabling efficient training. At each iteration, we sequentially update the network and discriminator parameters via gradient descent, refine the graph structure using a soft-threshold, compute the transformation matrices in closed form, project the auxiliary variable to satisfy non-negativity and no self-loops, and finally update the Lagrange multiplier.

3 Experiment

3.1 Experimental Preparation

To assess the performance of the AEGNet method for hyperspectral tumor diagnosis, we utilize the *In Vivo Hyperspectral Human Brain (In Vivo HHB)* dataset [3, 12]. Specifically, the In Vivo HHB dataset was gathered using a customized intraoperative hyperspectral acquisition system, enabling real-time identification of human brain tumors during neurosurgical procedures. This imaging setup employs a push-broom approach, spanning a spectral range of 400 to 1000nm with a spectral resolution of $2-3$nm, and capturing 826 spectral bands. The In Vivo HHB dataset comprises 36 MedHSIs from various patients, with each MedHSI classified into four categories: normal tissue, tumor tissue, blood vessel, and background elements.

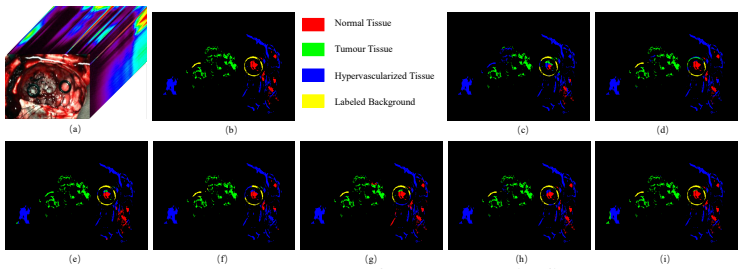

Fig. 2. Hyperspectral tumor diagnosis with classification maps of different methods with 0.5% ratio of training samples on MedHSI No. 020-01 (MedHSI-020-01) from the In Vivo HHB database. (a) Input MedHSI. (b) Ground truth. (c) SVM. (d) WSGraphCL. (e) FMDM. (f) FUST. (g) DMCA. (h) GiGCN. (i) Proposed AEGNet.

3.2 Algorithm Comparison

We here use the In Vivo HHB database recording numerous human brain cancers to evaluate the comparison between our proposed AEGNet method and the competing SVM, WSGraphCL [15], FMDM [6], FUST [20], DMCA [13], and GiGCN [9] approaches. There are numerous MedHSIs in the In Vivo HHB database, therefore we have randomly selected two MedHSIs including MediHSI No. 020-01 and MediHSI No. 015-01 as representative examples for the hyperspectral diagnosis comparison, where normal tissue, tumor tissue, hypervascularized tissue, and labeled background are included in each MedHSI. A 30 sampling factor has been employed to down-sample MediHSI No. 020-01 and MediHSI No. 015-01 along spatial dimension, which decreases the amount of spectral bands from 826 to 27 to reduce computational burden and conveniently observe the gap among

various diagnosis approaches. We have randomly chosen 0.5% in each category from each MedHSI as training samples, and the rest is designated as testing samples. The values of α, β, and γ included in the proposed AEGNet method are respectively set to 0.1, 0.001, and 0.01.

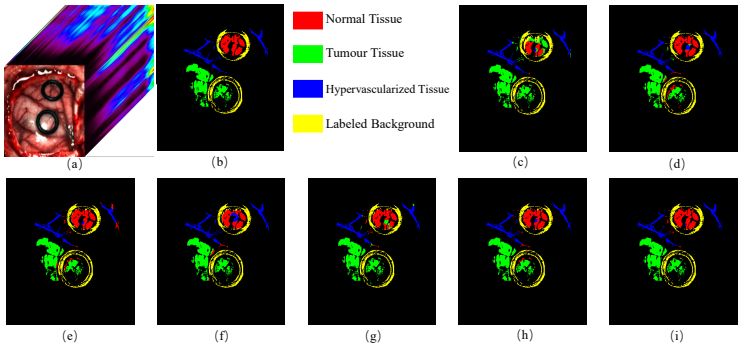

Fig. 3. Hyperspectral tumor diagnosis with classification maps of different methods with 0.5% ratio of training samples on MedHSI No. 020-01 (MedHSI-020-01) from the In Vivo HHB database. (a) Input MedHSI. (b) Ground truth. (c) SVM. (d) WSGraphCL. (e) FMDM. (f) FUST. (g) DMCA. (h) GiGCN. (i) Proposed AEGNet.

Table 1. Metric results of different approaches on MedHSI No. 015-01 (MedHSI-015-01) in the In-Vivo HHB database.

Class Name	Hyperspectral Tumor Diagnosis Methods						
	SVM	WSGraphCL	FMDM	FUST	DMCA	GiGCN	AEGNet
Normal Tissue	35.87	82.48	63.72	59.55	88.10	77.89	88.89
Tumour Tissue	84.04	95.67	100	98.04	95.38	96.71	100
Hypervascularized Tissue	98.51	99.78	92.12	99.74	94.37	97.79	94.65
Labeled Background	67.63	56.94	73.49	77.92	73.59	90.95	98.26
OA(%)	82.48	92.37	88.11	91.20	92.04	93.83	95.30
AA(%)	71.58	83.72	82.33	83.81	88.15	90.78	95.33
Kappa×100	70.89	87.82	81.43	85.82	87.68	90.29	92.78

Table 2. Metric results of different approaches on MedHSI No. 020-01 (MedHSI-020-01) in the In-Vivo HHB database.

Class Name	Hyperspectral Tumor Diagnosis Methods						
	SVM	WSGraphCL	FMDM	FUST	DMCA	GiGCN	AEGNet
Normal Tissue	46.39	91.34	92.88	78.77	87.68	93.08	96.56
Tumour Tissue	99.04	93.27	93.64	97.57	100	97.64	100
Hypervascularized Tissue	91.87	93.30	84.71	96.89	89.85	95.16	94.42
Labeled Background	98.21	99.73	99.96	99.92	99.50	99.81	100
OA(%)	87.62	94.67	93.81	94.52	95.92	96.97	98.28
AA(%)	83.22	94.41	92.80	93.29	94.26	96.42	97.62
Kappa×100	82.39	92.63	91.45	92.40	94.29	95.80	97.61

Table 1 and Table 2 are employed to show the OA, AA, and Kappa values of SVM, WSGraphCL, FMDM, FUST, DMCA, GiGCN, and proposed AEGNet for hyperspectral tumor diagnosis, where each presented value is averaged over the repeat of the experiment ten times. As can be directly seen from both tables, the OA, AA, and Kappa values of the proposed AEGNet method are consistently larger than those of SVM, WSGraphCL, FMDM, FUST, DMCA, and GiGCN. More intuitively, the accuracies of tumor tissue regions identified by the AEGNet method are the best. In addition, the classification maps of different methods

for hyperspectral tumor diagnosis are visually presented in Fig. 2 and Fig. 3 to further verify the superiority of the proposed AEGNet method to the six competing diagnosis strategies. In other words, the diagnosis maps generated by the AEGNet in Fig. 2(i) and Fig. 3(i) are more similar to the ground truths in Fig. 2(b) and Fig. 3(b), compared to those yielded via SVM, WSGraphCL, FMDM, FUST, DMCA, and GiGCN in Fig. 2(c)-(j) and Fig. 3(c)-(j). Based on the analysis above, it is demonstrated that our AEGNet method outperforms the six competing approaches in the hyperspectral tumor diagnosis on the brain cancer recorded In Vivo HHB database.

3.3 Ablation Study

The active evaluation component is introduced to dynamically evaluate whether the correlation between nodes is true and whether edges exist, which contributes to the construction of more accurate graph structures. To verify the effectiveness of the dynamic evaluation component, we initially eliminate it from the proposed AEGNet method and obtain a version without this component, referred to as AEGNet_NA. Subsequently, a comparison is implemented between AEGNet_NA and the original AEGNet, with the outcomes shown in Fig. 4(b). It is immediately apparent from the figure that the AEGNet achieves higher OA and Kappa values than AEGNet_NA. This indicates that, without the active evaluation component, there is no idea to ensure dynamic evaluation of edges between nodes, which limits the ability to construct graphs and achieve tumor diagnosis. Therefore, the active evaluation demonstrates its efficacy in AEGNet.

The hierarchical calibration is designed into the AEGNet to guarantee the hierarchical consistency between features of different layers. To validate the effectiveness of the hierarchical calibration component, we exclude it from the AEGNet, generating a variant without this component (denoted by AEGNet_NH). A comparison between AEGNet_NH and the original AEGNet is conducted, with the findings illustrated in Fig. 4(a). As can be revealed from this figure, the AEGNet method outperforms AEGNet_NH in terms of both OA and Kappa values. This is because, without the hierarchical calibration component, the AEGNet will become unable to guarantee hierarchical consistency between features of different layers, which limits the classification accuracy. Consequently, the hierarchical calibration component proves to be effective in AEGNet.

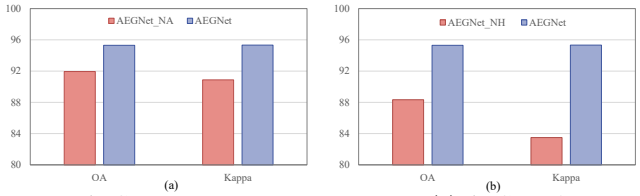

Fig. 4. The proposed AEGNet method is compared with: (a) AEGNet form without the active evaluation component (denoted by AEGNet_NA); (b) AEGNet form without the hierarchical calibration component (denoted by AEGNet_NH). The MedHSI-015-01 is used for the ablation, and the OA and Kappa are used to measure the results.

4 Conclusion

In this study, we present a novel active evaluation-induced graph network (AEGNet) based MedHSI classification for tumor diagnosis. Our proposal introduces two technical innovations: First, the active evaluation scheme is constructed by using an adversarial discriminator to determine the correlation and edge between nodes, which contributes to more precise graph construction. Second, considering the hierarchical misalignment possibly caused by inter-node misconnection of graph network, the hierarchical calibration loss is designed into the GNet architecture, which incentivizes all hidden features to align with the features of the final layer. Extensive experiments validate that AEGNet outperforms several representative methods in hyperspectral tumor diagnosis tasks on the brain cancer recorded In Vivo HHB database.

Acknowledgments. This work was supported by the National Natural Science Foundation of China (Nos: 62572254, 62101247, 62106104, 62301111), the Funded by Basic Research Program of Jiangsu (No: BK20251875), the Guangdong Basic and Applied Basic Research Foundation (No: 2026A1515012246), and the Shenzhen Science and Technology Program (No: JCYJ20250604191403006).

Disclosure of Interests. The authors have no competing interests to declare that are relevant to the content of this article.

References

1. Bai, L., Cui, L., Jiao, Y., Rossi, L., Hancock, E.R.: Learning backtrackless aligned-spatial graph convolutional networks for graph classification. IEEE Trans. Pattern Anal. Mach. Intell. **44**(2), 783–798 (Feb 2022)
2. Dong, Y., Liu, Q., Du, B., Zhang, L.: Weighted feature fusion of convolutional neural network and graph attention network for hyperspectral image classification. IEEE Trans. Image Process. **31**, 1559–1572 (Jan 2022)
3. Fabelo, H., Ortega, S., Szolna, A., Bulters, D., Piñeiro, J.F., Kabwama, S., JO'Shanahan, A., Bulstrode, H., Bisshopp, S., Kiran, B.R., et al.: In-vivo hyperspectral human brain image database for brain cancer detection. IEEE Access **7**, 39098–39116 (Apr 2019)
4. Guang, M., Yan, C., Xu, Y., Wang, J., Jiang, C.: Graph convolutional networks with adaptive neighborhood awareness. IEEE Trans. Pattern Anal. Mach. Intell. **46**(11), 7392–7404 (Nov 2024)
5. Halicek, M., Lu, G., Little, J.V., Wang, X., Patel, M., Griffith, C.C., El-Deiry, M.W., Chen, A.Y., Fei, B.: Deep convolutional neural networks for classifying head and neck cancer using hyperspectral imaging. J. Biomed. Opt. **22**(6) (Jun 2017), art. no. 060503
6. Hao, Q., Pei, Y., Zhou, R., Sun, B., Sun, J., Li, S., Kang, X.: Fusing multiple deep models for in vivo human brain hyperspectral image classification to identify glioblastoma tumor. IEEE Trans. Instrum. Meas. **70**, 1–14 (2021)
7. Hu, B., Du, J., Zhang, Z., Wang, Q.: Tumor tissue classification based on micro-hyperspectral technology and deep learning. Biomed. Opt. Express **10**(12), 6370–6389 (Dec 2019)

8. Jeyaraj, P.R., Samuel Nadar, E.R.: Computer-assisted medical image classification for early diagnosis of oral cancer employing deep learning algorithm. J. Cancer Res. Clin. **145**(4), 829–837 (Jan 2019)
9. Jia, S., Jiang, S., Zhang, S., Xu, M., Jia, X.: Graph-in-graph convolutional network for hyperspectral image classification. IEEE Trans. Neural Netw. Learn. Syst. **35**(1), 1157–1171 (Jan 2024)
10. Li, X., Li, W., Xu, X., Hu, W.: Cell classification using convolutional neural networks in medical hyperspectral imagery. In: Proc. IEEE Int. Conf. Image Vis. Comput. (ICIVC). pp. 501–504 (2017)
11. Lv, M., Liu, S., Ma, X., Yang, Y., Zhang, H., Li, W.: Medical hyperspectral image feature selection framework using functional data analysis: Application to membranous nephropathy pathologic diagnosis. IEEE J. Biomed. Health Inform. **29**(10), 7409–7422 (Jul 2025)
12. RavÃň, D., Fabelo, H., Callic, G.M., Yang, G.Z.: Manifold embedding and semantic segmentation for intraoperative guidance with hyperspectral brain imaging. IEEE Trans. Med. Imag. **36**(9), 1845–1857 (Apr 2017)
13. Wang, M., Xu, Y., Wang, Z., Xing, C.: Deep margin cosine autoencoder-based medical hyperspectral image classification for tumor diagnosis. IEEE Trans. Instrum. Meas. **72**, 1–12 (Jul 2023)
14. Wang, Q., Sun, L., Wang, Y., Zhou, M., Hu, M., Chen, J., Wen, Y., Li, Q.: Identification of melanoma from hyperspectral pathology image using 3d convolutional networks. IEEE Trans. Med. Imag. **40**(1), 218–227 (Jan 2021)
15. Wang, S., Braham, N.A.A., Zhu, X.X.: Weak-strong graph contrastive learning neural network for hyperspectral image classification. IEEE Trans. Geosci. Remote Sens. **63**, 1–17 (May 2025)
16. Wei, X., Li, W., Zhang, M., Li, Q.: Medical hyperspectral image classification based on end-to-end fusion deep neural network. IEEE Trans. Instrum. Meas. **68**(11), 4481–4492 (Nov 2019)
17. Xie, Y., Han, L., Cai, W., Shao, X.: Enhanced bi-branch deep learning network for in vivo hyperspectral imaging recognition of organs and tissues. Spectrochimica Acta Part A: Molecular and Biomolecular Spectroscopy **345**, 126815 (Jan 2026)
18. Yuan, Y., Ma, D., Wang, Q.: Hyperspectral anomaly detection by graph pixel selection. IEEE Trans. Cybern. **46**(12), 3123–3134 (Dec 2016)
19. Yun, B., Lei, B., Chen, J., Wang, H., Qiu, S., Shen, W., Li, Q., Wang, Y.: Spectr: Spectral transformer for microscopic hyperspectral pathology image segmentation. IEEE Trans. Circuits Syst. Video Technol. **34**(6), 4610–4624 (Jun 2024)
20. Zeng, W., Li, W., Zhang, M., Wang, H., Lv, M., Yang, Y., Tao, R.: Microscopic hyperspectral image classification based on fusion transformer with parallel cnn. IEEE J. Biomed. Health Inform. pp. 2910–2921 (Jun 2023)